Surface structure and segregation profile of the alloy $Au_3Pd(110)$: Experiment and theory

J. Kuntze, S. Speller, and W. Heiland
Universität Osnabrück, FB Physik, D-49069 Osnabrück, Germany

P. Deurinck and C. Creemers
Fysico-chemisch Laboratorium, Katholieke Universiteit Leuven, W. de Croylaan, B-3001 Leuven, Belgium

A. Atrei
Dipartimento di Scienze e Tecnologie Chimiche e dei Biosistemi, Università di Siena, 53100 Siena, Italy

U. Bardi
Dipartimento di Chimica, Università di Firenze, 50121 Firenze, Italy
(Received 5 May 1999)

The (110) surface of the alloy Au_3Pd has been investigated by quantitative low-energy electron diffraction and low-energy ion scattering spectroscopy to determine the structure and composition of the first three atomic layers. The structure and the segregation profile have also been modeled by means of the embedded atom method, combined with Monte Carlo simulations. Both the experimental and theoretical results indicate segregation of gold, resulting in (nearly) pure Au in the two topmost layers. The surface is (1×2) missing-row reconstructed similarly to Au(110), with a significant contraction of the first interlayer spacing and a buckling in the third layer. [S0163-1829(99)01636-7]

I. INTRODUCTION

The study of metal alloy surfaces has gained increasing interest in recent years owing to their applications in technology and catalysis.[1–3] For AuPd alloys, catalytic activity regarding CO oxidation and decomposition of N_2O and formic acid has been reported.[1] To understand the mechanisms responsible for the catalytic processes, a detailed characterization of the surface structure and composition is necessary. For Au-containing alloys such as $Cu_3Au(110)$,[4] $Cu_3Au(001)$,[4,5] $Au_3Cu(001)$,[6] $Au_3Pd(113)$,[7] and $Au_3Pd(001)$,[8,9] Au segregation is always found. But the details of the segregation and reconstruction processes are still not completely understood. For example, the topmost layer of the $Au_3Pd(001)$ surface consists of pure Au but is not reconstructed like Au(001), which exhibits a quasi-hexagonal structure with a $c(26\times68)$ low-energy electron diffraction (LEED) pattern.[10] On the other hand, for the (001) surface of Pt_xNi_{1-x} alloys,[11] an increasing tendency to form reconstructions such as pure Pt(001) (Refs. 10 and 12) has been found with increasing Pt concentration in the topmost layer. The same can be said for (110) surfaces of Pt-containing alloys such as $Pt_{25}Rh_{75}(110)$ (Ref. 13) and $Pt_{80}Fe_{20}(110)$, [14] which exhibit a (1×2) missing-row reconstruction as Pt(110).[15] As is known, Au(110) reconstructs in the same way.[16–18]

The aim of the present paper is therefore to investigate the structure and composition of $Au_3Pd(110)$ using quantitative LEED and low-energy ion scattering spectroscopy (LEIS). The structure and composition have also been calculated with Monte Carlo (MC) simulations combined with the embedded atom method (EAM). The remainder of this paper is divided into four main parts, dealing with the experiment (Sec. II) and the simulations (Sec. III), followed by the discussion (Sec. IV) and a summary (Sec. V).

II. EXPERIMENT

Prior to the vacuum experiments, the lattice constant and ordering of the sample was checked with x-ray diffraction (XRD). We found a substitutionally disordered sample with a lattice constant of 4.01 Å.

The other experiments were performed in a vacuum chamber with base pressures in the 10^{-8} Pa range. The chamber was equipped with a hemispherical electron analyzer (modified for the detection of ions) and two-grid optics for LEED. X-ray photoelectron spectra (XPS) were recorded during the first stages of the preparation to check for surface impurities. Subsequent checks were performed by ion scattering. LEIS spectra were taken with 1 keV He^+ or Ne^+ with sample currents of 16–18 nA. The scattering angle was 135°, and the incidence angle was 45°. For sputtering, we use 500 eV–1 keV Ar^+ ions with sample currents up to 5 μA. During sputtering the beam was scanned over the sample.

The LEED intensity (I-V) curves were measured using a video LEED system in an energy range from 50–400 eV. The I-V curves were acquired for 13 sets of nonequivalent beams at normal incidence of the primary electron beam. The I-V curves for the symmetrically equivalent beams were averaged in order to compensate for the residual minor discrepancies in the normal-incidence condition. Intensities were normalized to constant incident current, and the background was estimated from measurements of the intensity in the proximity of the spots and substracted from the I-V curves.

A. LEED calculations

Dynamical calculations of the LEED intensities were performed using the Barbieri–Van Hove symmetrized automated tensor LEED package.[19] The scattering by Au and Pd atoms was described using 11 phase shifts, derived from a muffin-tin potential calculated for the Au_3Pd alloy using the Barbieri–Van Hove phase-shift package.[20] The bulk Debye temperatures for Au and Pd used in the calculations were 165 K and 274 K, respectively.[21] Calculations using an enhanced vibrational amplitude at the surface have not been done. The average *t*-matrix approximation[22] was used to calculate the effect of random enrichment in one of the components. The real part of the inner potential was set to 10 V and optimized in the *R* factor analysis. The imaginary part of the inner potential was set to 5 V. The calculations were performed in an energy range from 80–380 eV.

Calculations were done for a grid of varying compositions of the first three layers using a nonrelaxed missing-row structure as the reference structure [which is justified by the (1×2) reconstruction apparent in the LEED pattern, see Sec. II B, and the fact that Au(110) is missing-row reconstructed]. For each composition, the first three interlayer distances were then optimized in the second step of the TLEED calculations[19] to get the best agreement with the experimental *I-V* curves. This procedure was repeated with refined reference structures until the displacements of the atoms were $\leqslant 0.02$ Å in the fitting procedure, ensuring convergence. As a last step, pairing was allowed in the second layer. In the *R* factor analysis, the R_P (Pendry) and R_{MZJ} (modified Zanazzi-Jona) reliability factors[23] and an average of the two were used. The total-energy range used in the calculations was 2311 eV, and the error bars for the values of the structural parameters were estimated from the variance of the R_P factor,[24] using the formula $\Delta R = R_{\min}(8V_{0i}/\Delta E)^{1/2}$, where $R_{\min}$ is the minimum of the R_P, V_{0i} is the imaginary part of the inner potential, and ΔE is the total-energy range. The error bars for the layer composition was estimated in the same way, holding all structural parameters and the compositions of the other layers at best-fit values.

B. Experimental results

After several cleaning cycles using 500 eV–1 keV Ar^+ followed by annealing to 770 K for 10 min, no contaminants could be detected by XPS and LEIS. The LEED pattern indicates a (1×2)-surface unit cell.

LEIS spectra taken with 1 keV He^+ (Fig. 1) show segregation of Au upon annealing, with virtually no residual Pd signal for the annealed surface. The Pd signal increases with increasing ion dose, so we conclude that the traces of residual Pd are due to sputtering during the acquisition time (the time for one spectrum is approximately 5 min). The spectra recorded directly after Ar^+ sputtering show a clear Pd signal, which amounts to approximately 30–35 at. %, taking into account the respective scattering cross sections for Au and Pd and using the sensitivity factors for polycrystalline materials.[25] This is higher than the bulk concentration, but regarding the uncertainty in the neutralization probabilities, the deviation is within the error limits. Since no elemental standards were available for our experiments, quantification of LEIS should be regarded as an approximation only.

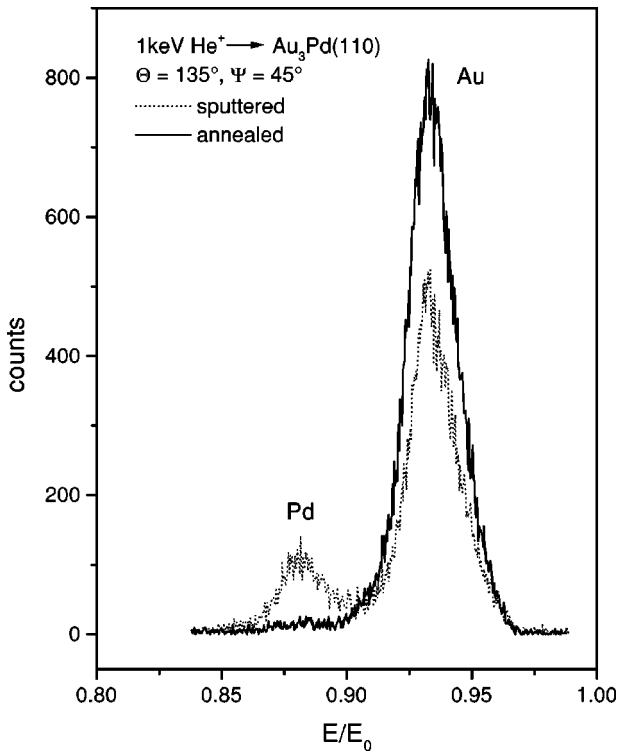

FIG. 1. LEIS spectra (raw data) taken with 1 keV He^+ after sputtering (dotted line) and annealing to 770 K (solid line). The spectra have been acquired at constant pass energy.

We note, however, that in previous studies Pd enrichment during sputtering has been found for polycrystalline alloys of AuPd.[26]

For an open surface such as (110) (especially if it is reconstructed), a contribution from the second layer cannot be excluded for the scattering parameters used (angle of incidence 45°, scattering angle 135°) but is believed to be small due to the high neutralization probability in the first and second layer.[27] We attribute the signal mainly to the first layer, which is obviously pure Au. The contribution from the second layer cannot be quantified exactly, but since the LEIS signal shows only Au, we conclude that also the second layer is pure Au. For an exact determination of the second layer composition, a series of LEIS spectra (preferentially using a time-of-flight system to detect neutral particles) with varying angles of incidence would be necessary, which have not been performed in the present analysis.

For the LEED calculations, a grid of different layer compositions has been tested: the Au concentration, as atomic fraction, in the first three atomic layers has been varied from 0–1 in steps of 0.1, with bulk concentration in all deeper layers. At each composition, a fit of the structural parameters was done. At best-fit values the Pendry *r* factor was $R_P = 0.273$ ($R_{\mathrm{MZJ}} = 0.135$); all *r* factors indicate the same minimum within the error limits. With regard to the composition, the same minimum has been reached using the R_P and the R_{MZJ}. The final results are listed in Table I; for a visualization of the structural parameters, see Fig. 2. the first interlayer spacing is contracted by 0.19 Å, and the second interlayer spacing is slightly expanded by 0.01 Å, which is within the error limits of the analysis. Note that all interlayer spacings refer to the center-of-mass planes (see also Fig. 2).

TABLE I. Structure and composition for $Au_3Pd(110)$, determined by LEED (best-fit values for $R_P=0.273$) and MC-EAM calculations (simulations III, Fig. 8, values for 300 K). For an explanation of the parameters see Fig. 2. For comparison, the values for the (1×2) reconstructed Au(110) surface taken from Ref. 17 are given. All interlayer distances refer to center-of-mass planes. The error bars have been estimated using the variance of the Pendry *R* factor (compare Figs. 4 and 5); they apply only to the experimental data.

Parameter	$Au_3Pd(110)$ expt./sim	Au(110)	Error bars
d_{12}	1.23 Å/1.29 Å	1.15 Å	0.04 Å
d_{23}	1.43 Å/1.43 Å	1.47 Å	0.04 Å
Δz_3	0.14 Å/0.03 Å	0.24 Å	0.04 Å
d_{34}	1.41 Å/1.41 Å	1.47 Å	0.04 Å
Δy_2	0.01 Å	0.07 Å	0.07 Å
d_{bulk}	1.418 Å	1.442	fixed
c_1	1.0/0.96		0.13
c_2	1.0/0.94		0.13
c_3	0.5/0.83		+0.35/−0.25
c_{bulk}	0.75		fixed

The third layer is buckled by 0.14 Å, and a slight pairing of 0.015 Å in the second layer could be present, the latter being also within the error limits. For the composition, best agreement was achieved with $c_{1,2}=1.00$ and $c_3=0.50$ (the index denotes the atomic layer). With regard to the composition, no variations within the buckled third layer have been allowed. Variation of the layer composition in proximity of the minimum found in the coarse grid did not further improve the fit.

To check consistency with the XRD lattice-constant measurements, a_0 has also been varied. The best agreement has been achieved for 4.01 Å, i.e., for the same lattice constant that has been found in the XRD experiment.

The comparison of the experimental and the theoretical curves is shown in Fig. 3. The sensitivity of the R_P factor to the structural parameters and to the composition is shown in Figs. 4 and 5, respectively. The final structure and composition is listed in Table I.

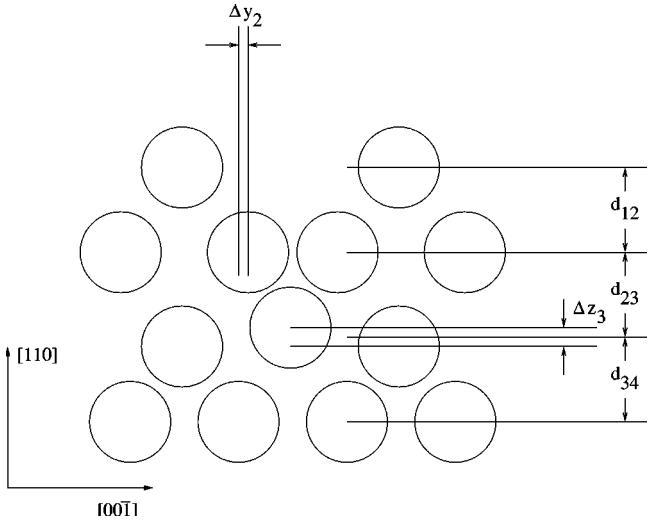

FIG. 2. Schematic missing-row model of the (1×2) reconstruction (relaxations are not in scale). The structural parameters that were optimized in the fitting procedure are indicated. For the results see Table I.

III. THEORY

A. Theoretical background

The aim of this paper is to explain and understand the segregation behavior at the $Au_3Pd(110)$ surface in an analytical way. It is assumed that the experimentally observed surface structure and surface concentrations are real equilibrium configurations that can be modeled by minimizing the Gibbs energy $(\Delta H-T\Delta S)$. These minima are computed by Monte Carlo simulations.[28–32] The stochastic nature of these simulations reflects the entropy part (ΔS). In principle, the (alloy) energy can be computed by solving the many-electron Schrödinger equation. In practice, however, it is recommended to approximate the energy, yet retaining enough information about the underlying physics to describe even minor energy effects. The embedded atom method is used for modeling the enthalpy part (ΔH). We have chosen the MC-EAM combination because of its successful application to other alloys.[33–35] In the next sections, the Monte Carlo method and the embedded atom method are described in more detail.

1. Monte Carlo simulations

The Monte Carlo method is based on statistical mechanics and aims to explain the macroscopic observable properties of a system in terms of the underlying microscopic behavior. A macroscopic quantity $A(S)$ of the system S is given by

$$A(S)=\frac{\int_{\Omega(S)}A(X)f(X)}{\int_{\Omega(S)}f(X)} \tag{1}$$

with the state phase $\Omega(S)$ collecting all possible states X for the system S, and $f(X)$ expressing the probability for the occurrence of state X. In order to make the above formula amenable to computer simulations, the integral has to be converted into an averaged sum over a finite number of well-chosen representable states. This is accomplished through the Monte Carlo method, which makes use of random numbers to generate a finite set of states X. The Monte Carlo method used here is the Metropolis method,[28] which produces a first-order Markov sequence of states $X_0, X_1, \ldots, X_\delta, \ldots, X_{\delta+n-1}$. The probability of evolving from state X_i to state X_j denoted by $P_{ij}=f(X_j)/f(X_i)$. The interstate transition probabilities are quantified so that after a sufficient number of steps δ the probability of the simulated system to be in a given state X_i equals the true $f(X_i)$, independent of the initial state X_0. The macroscopic property $A(S)$ can then be approximated by

$$A(S)=\frac{1}{n}\sum_{k=\delta}^{k=\delta+n-1}A(X). \tag{2}$$

In the Monte Carlo simulations, the segregation processes and possible surface relaxations and reconstructions are

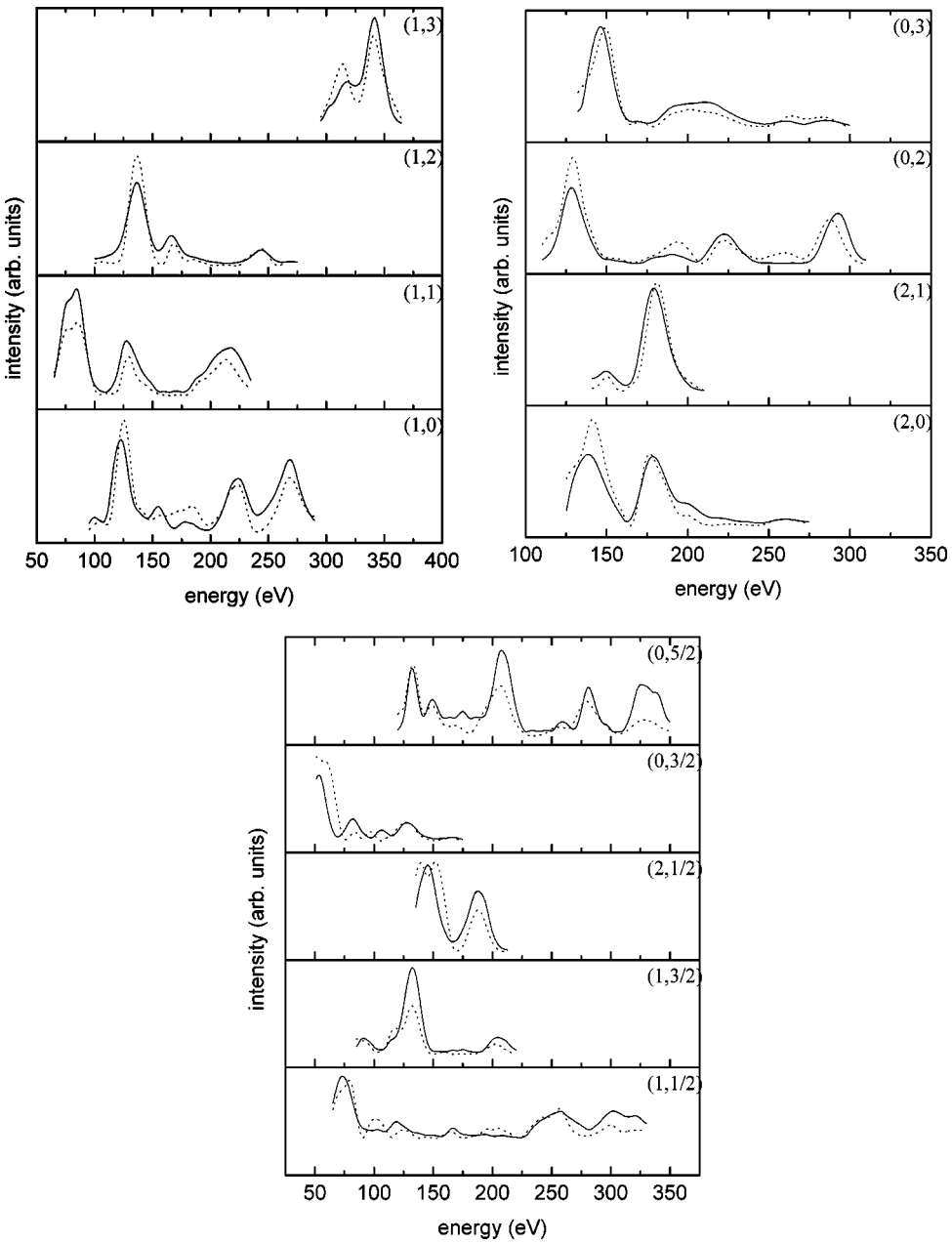

FIG. 3. Comparison between experimental (solid lines) and calculated (dotted lines) I-V-curves. All data are aquired at normal incidence. The calculated curves correspond to the minimum of the R factor analysis.

mimicked by considering a change in the chemical identity of the atoms and a slight displacement from their original bulklike position. To compute the distribution function $f(X)$, two approaches exist: the *canonical ensemble* and the *grand canonical ensemble*.

In the *canonical ensemble* the number of atoms of each element, the volume, and the temperature remain constant. The simulation proceeds by interchanging two randomly picked atoms of a different kind. The probability of state X_x is then given by the Boltzmann distribution

$$f(X_x)=P_x=e^{-E_x/kT} \tag{3}$$

with E_x denoting the energy of the configuration x, T the temperature, and k is the Boltzmann constant. Determining the probability P_{xy} of evolving from state X_x to state X_y then is merely reduced to computing the energy difference between the states X_x and X_y,

$$P_{xy}=f(X_y)/f(X_x)=e^{-(E_y-E_x)/kT}. \tag{4}$$

In the grand canonical ensemble the total number of atoms, the temperature, and the difference in chemical potential $(\Delta\mu)$ between two species are held fixed. The simulation proceeds by picking an atom and by considering to change its identity. The latter ensures consistency between the surface composition and the bulk composition. The probability of state X_x is then given by

$$f(X_x)=P_x=(V/\Lambda_A^3)^{N_A}(V/\Lambda_B^3)^{N_B}e^{-(E_x-N_A\mu_A-N_B\mu_B)/kT} \tag{5}$$

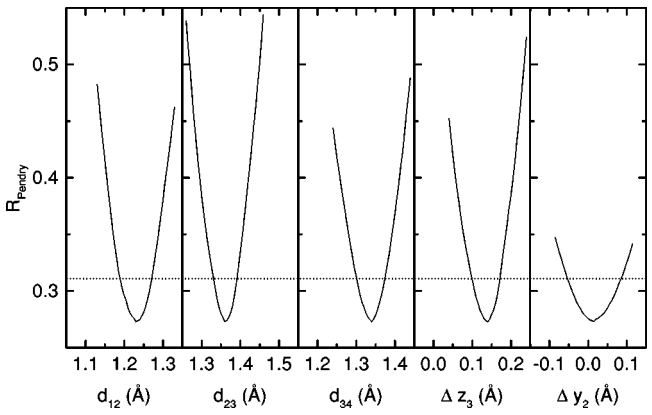

FIG. 4. Pendry R factor as a function of the structural parameters. The dotted horizontal line indicates the limit for a significant change in the R_P factor.

with V denoting the constant volume of the system, E_x denoting the energy of configuration x, T is the temperature, k is the Boltzmann constant, N_A is the number of A atoms, N_B is the number of B atoms, Λ_i and μ_i, respectively, denote the thermal de Broglie wavelength and the chemical potential of element i.

The probability P_{xy} of evolving from state X_x to state X_y, where an A atom is replaced by an atom B, is then given by

$$P_{xy}=f(X_y)/f(X_x)=(\Lambda_A^3/\Lambda_B^3)e^{-(\Delta E+\Delta\mu)/kT}. \tag{6}$$

In both the canonical ensemble and the grand canonical ensemble, the decision of whether or not a state transition is accepted is made by comparing the transition probability with a random number between 0 and 1. Providing an accurate energy model is used, a correct equilibrium configuration will be reached eventually, without *a priori* assumptions.

As already pointed out in Sec. II, several changes occur near the $Au_3Pd(110)$ surface. Besides the compositional rearrangements, reconstructions and relaxations also play an important role. These can be incorporated in both simulation schemes. In principle, vibrations can be incorporated as well.

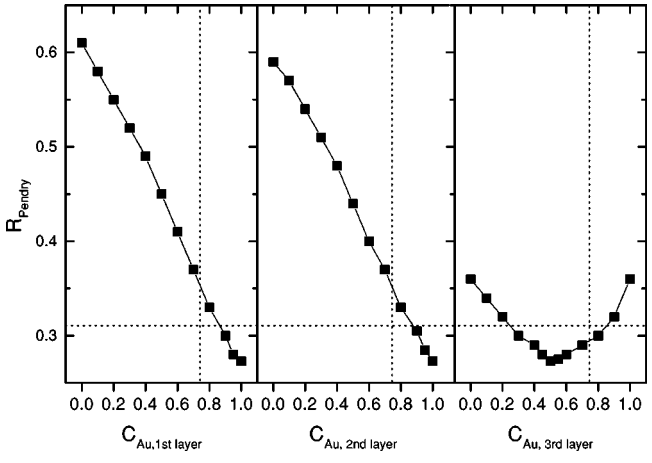

FIG. 5. Pendry R factor as a function of the composition in the first three layers. The dotted vertical lines indicate the bulk composition. The dotted horizontal line indicates the limit for a significant change in the R_P factor.

In the grand canonical ensemble, however, this would be extremely time consuming due to the iterative procedure to determine $\Delta\mu$. The simulations in this paper are therefore based on the canonical ensemble. To alleviate the finite-size effects, the slab of atoms is taken sufficiently large, so that the composition of the deeper layers converges to the real bulk composition. For details, we refer to Sec. III B.

2. Embedded atom method

The embedded atom method defines the energy E_i of an atom i in a lattice as the sum of the energy due to electrostatic interactions with its neighbors and the energy needed to embed this atom in the local electron density as generated by the other atoms in the system. This embedding energy depends only on the nature of atom i and can hence be derived from material constants of pure i. The energy of a configuration x is then defined as the sum of the energies of the atoms within x:[36]

$$E_x=\sum_i E_i=\sum_i \left(F_i(\rho_{h,i})+0.5\sum_j \Phi_{ij}\right), \tag{7}$$

where F_i is the embedding energy function of atom i, $\rho_{h,i}$ is the host electron density around atom i due to the other atoms, and Φ_{ij} is the electrostatic interaction energy between atoms i and j. The host electron density $\rho_{h,i}$ is obtained by summing the contributions of all the neighbors j of atom i,

$$\rho_{h,i}=\sum_j \rho_j\,. \tag{8}$$

In practice, the ρ_j functions and the Φ_{ij} functions are represented by parametrized analytical expressions. In this paper, we employ the parametrization of Foiles, Baskes, and Daw.[36] The electron density of atom $j(\rho_j)$ is computed by means of the Hartree-Fock wave functions.[37,38] To account for possible electronic rearrangements upon alloying, the fixed total number of outer electrons of element j (N_j) is allowed to redistribute over the s and d sublevels. More precisely, ρ_j is modeled as

$$\rho_j=n_{s,j}\rho_{s,j}+(N_j-n_{s,j})\rho_{d,j}\,, \tag{9}$$

where $n_{s,j}$ denotes the number of outer s electrons, and $\rho_{s,j}$ and $\rho_{d,j}$ are the densities associated with the s and d ground-state wave functions, respectively. The pair interaction term Φ_{ij} is calculated as the electrostatic Coulomb repulsion between the screened effective nuclear charges[36]

$$\Phi_{ij}=(1/4\pi\epsilon_0)Z_i(R_{ij})Z_j(R_{ij})/R_{ij} \tag{10}$$

with R_{ij} denoting the distance between the atoms i and j, and Z_i being the effective charge of atom i:

$$Z_i(R)=Z_{0,i}(1+\beta_i R_i^{\nu_i})e^{-\alpha_i R}, \tag{11}$$

where $Z_{0,i}$ denotes the number of outer electrons of atom i, α_i and β_i are parameters to be determined, and ν_i is a parameter that is empirically taken equal to 1 or 2.

The derivation of the parameters $n_{s,i}$, α_i, and β_i, for each element i, is detailed in Ref. 34. Basically, a least-square optimization is set up to solve an overdetermined set of equations. For each element, the parameter values are op-

timized so as to yield the elastic constants and vacancy formation energy of each material as well as the dilute limits of the heats of solution of the binary alloys. We have used the parameter values reported in Ref. 36. These values are optimized towards alloy systems containing Cu, Pd, Pt, Ni, Ag, and Au.

Once the atomic electron densities ρ_j and the pair interactions Φ_{ij} are known, the embedding energy function F_i is derived by considering the pure metal i. At equilibrium (lattice constant a_0), the energy of this pure metal is given by the sublimation energy $-E_{\mathrm{sub}}$; in expanded or compressed form (lattice constant a), the energy of this configuration is given by Rose's universal equation of state:[39]

$$E(a) = -E_{\mathrm{sub}}(1+a')e^{-a'}, \tag{12}$$

where a' denotes the relative deviation from the equilibrium lattice constant a_0 or

$$a' = (a/a_0 - 1)/(E_{\mathrm{sub}}/9B\Omega)^{1/2}, \tag{13}$$

where B is the bulk modulus of pure i and Ω the equilibrium volume per atom. By setting Eq. (7) equal to Eq. (12), F_i is readily obtained.

B. Simulations

The equilibrium situation is calculated for temperatures of 300 K, 600 K, and 800 K. These temperatures are chosen because the sample preparation included an annealing at 770 K. Although the measurements are done at room temperature, the sample is in the frozen equilibrium state, corresponding to the temperature where the atomic mobility was lost, typically one third of the melting point.

The MC-EAM simulations are performed according to the canonical ensemble for temperatures of 300 K, 600 K, and 800 K. First and second neighbor interactions are accounted for. The Au_3Pd alloy is modeled as a three-dimensional lattice of eight layers of 560 atoms each, with periodic boundary conditions to minimize finite-size effects. To eliminate the influence of the initial configuration, the results of the first million simulation steps are simply discarded; the results of the subsequent million steps are sampled with an interval of 5.000 steps. The simulation program is implemented in C and executed on a Pentium II platform.

Simulations are also performed to derive the degree of bulk order and to characterize the changes in the surface layers. In the next sections, these simulations are described in more detail.

1. Bulk simulations

The quasi-infinite bulk (without a surface) is mimicked by applying periodic boundary conditions along all three orthogonal directions. The aim is to derive the degree of order in the bulk. Hereby, the order is quantified by the long-range order (S) figure. This figure assumes the alloy lattice is divided into two sublattices α and β. In a perfectly long-range ordered Au_3Pd alloy ($S=1$), all $\alpha(\beta)$ sites are occupied by Au (Pd) atoms; in a completely disordered Au_3Pd alloy ($S=0$), the probability of α and β sites being occupied by an Au atom is equal to 0.75, the Au bulk fraction.

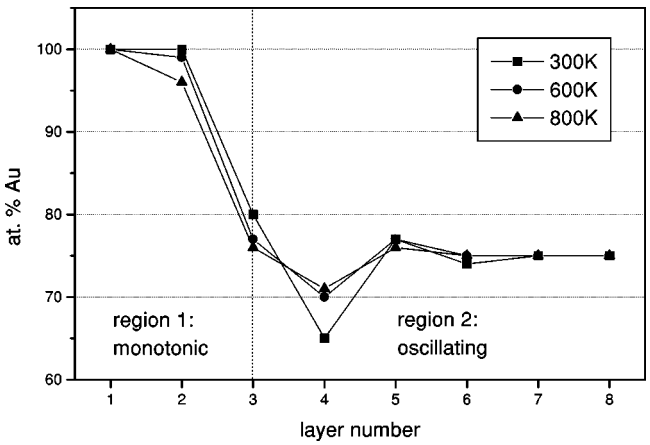

FIG. 6. Au concentration at different temperatures as a function of depth according to simulation I: bulk truncated surface.

Even starting from a perfectly chemically ordered initial configuration, the simulations arrive at a disordered bulk ($S \approx 0$) at 300 K—in complete agreement with our XRD data.

2. Surface simulations

The quasi-infinite bulk is modeled by applying periodic boundary conditions along the directions perpendicular to the (110) surface. The initial configuration is a complete disordered lattice (see Sec. III B 1). For efficiency reasons, only the eight upper layers are subject to changes; the other layers are left unchanged. This is amply sufficient since surface segregation and relaxation are known to be confined to a few outermost layers.

The aim is to derive the composition and the relaxation in the surface layers and to gain better insight from the comparison with the experimental results of Sec. II. Three different series of simulations are performed.

(a) *Simulation I: the unreconstructed (110) surface*. In the first simulations, the atoms of the full (110) layer are not allowed to move from their equilibrium positions. For 300 K, 600 K, and 800 K, the composition profiles of Fig. 6 are obtained.

In Fig. 6, two regions can be distinguished: The first monotonic region (layers 1, 2, 3) with pure Au in the first and second layer and the second oscillating region (layers 3–8). From the third layer on, one observes the normal damped oscillatory concentration profile that is expected for an alloy with a negative (exothermic) heat of mixing. In such an alloy AB-bonds are energetically preferred, and this can ultimately lead to the formation of chemically ordered intermetallic compounds.

In less exothermic alloys as in Au-Pd, the weaker A-B attractions generate these composition oscillations only at the surface: the segregation enrichment is modulated with these oscillations, whereas in endothermic alloys a monotonic decay of the surface enrichment is observed. Both situations are like reminders of the demixing into two phases for endothermic alloys (repulsive A-B interactions) and the formation of stoichiometric and ordered compounds in exothermic alloys (A-B attractions). Au segregates, driven by its considerably lower surface energy: with EAM one calculates 0.98 J/m^2 for Au compared to 1.49 J/m^2 for Pd.

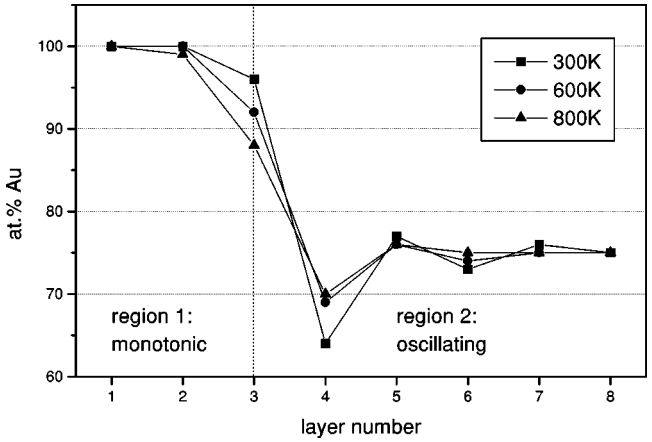

FIG. 7. Au concentration at different temperatures as a function of depth according to simulation II: (1×2) missing-row reconstructed surface with no relaxations.

The monotonic Au enrichment on top of the oscillating profile is also generated by this large difference in surface energy that is felt up to the third atomic layer, two layers deeper than in the simple treatment with pairwise interactions between the nearest neighbors only in a closed-packed (111) surface.[40] On the one hand, the second layer of a (110) surface is still part of the surface because its atoms also have an incomplete coordination. On the other hand, EAM also takes next-nearest-neighbor interactions into account, which again extends the influence of the surface one layer deeper than with nearest-neighbor interactions only. The normal oscillatory profile is therefore delayed until the third layer. The influence of the corrugated (110) surface on the segregation profile is substantiated by our EAM simulations for the (111) surface where the oscillations start one layer earlier, from the second layer on.

(b) *Simulation II: the (110) surface with the* (1×2) *missing-row reconstruction.* In order to allow an even better comparison with the experiments, where LEED shows a (1×2) surface reconstruction, a second series of simulations was set up on a slab in which the atoms are still fixed at their lattice sites, but with a missing-row configuration at the surface. Comparison of the total EAM energy of the unreconstructed slab and the slab with the reconstructed surface proves that the missing-row model lowers the energy and thus corresponds to a more stable situation. The simulations for the three temperatures yield the segregation profiles of Fig. 7.

The profiles are quite comparable to those of Fig. 6, except for a significantly higher Au concentration in the third layer. The explanation is straightforward: due to the missing rows and an increased number of missing neighbors, the surface character of the second and third layer has become stronger. The surface energy effect then extends more deeply and causes also the third layer to become enriched in Au.

(c) *Simulation III: the (110) surface with the* (1×2) *missing-row reconstruction and relaxations.* The third series of simulations also start from a (1×2) missing-row reconstructed surface but now takes surface relaxations into account by allowing small displacements of the atoms from their normal lattice positions. The composition profiles of Fig. 8 are obtained.

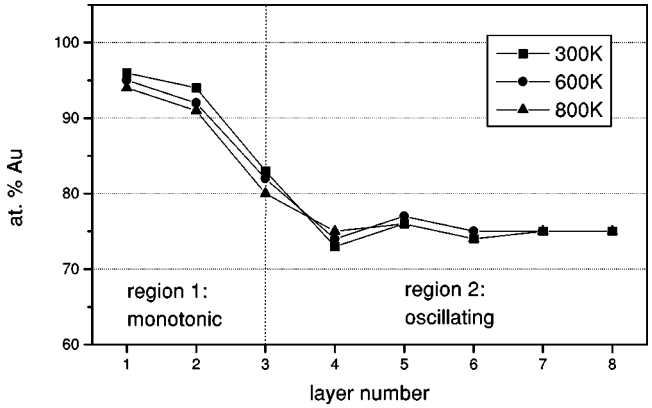

FIG. 8. Au concentration at different temperatures as a function of depth according to simulation III: the (1×2) missing-row reconstructed surface and surface relaxations.

Clearly the relaxations at the surface have diminished the extent of segregation and have ''flattened'' the profiles of Fig. 7. The computed interlayer spacings are 1.29 Å between the first and second layer and 1.43 Å between the second and third layer. Compared with the bulk layer spacing of 1.418 Å, one concludes a contraction between the first and the second layer and a small expansion between the second and the third layer.

These observations are both normal and coupled: at the surface the Gibbs energy is minimized by electronic redistributions. The resulting relaxation in the surface bond energies, in turn, gives rise to both a lower surface energy and a structural relaxation: the incomplete coordination of the surface atoms causes a bond strengthening of the remaining bonds at the expense of the missing bonds. Hence the surface energy, that can crudely be estimated at one-half the energy in the missing bonds, is lowered. The reduced (difference in) surface energy, in turn, leads to a less pronounced segregation. At the same time, the reinforcement of the bonds between the surface layers is accompanied by a bond shortening, and one observes a contraction between the first and the second layer. The bond strengthening between layers one and two then again induces a bond weakening between layers two and three, which causes an increased interlayer spacing between the second and third atomic layer in a contraction-expansion sequence, that is typical for the surfaces of metals and alloys. In the third layer a slight buckling (0.03 Å) is observed, caused by an upward displacement of the atoms under the missing rows.

IV. DISCUSSION

The agreement between theory and experiment for the LEED experiments is within the limits for a satisfactory structural determination. Both LEIS and LEED indicate a first layer composition of pure Au. According to LEED, the second layer also consists of pure Au, with 87–100 at. % being the possible range that is compatible with an insignificant change in the Pendry *r* factor. We note that the estimate of error bars for compositional changes using the variance of the Pendry *r* factor may be regarded as an upper limit. For very good agreement between theory and experiment [e.g., R_P well below 0.2 for a (100) surface[41]], a higher sensitivity can be obtained. However, due to stray magnetic fields during our experiments leading to minor deviations from the

normal-incidence condition, we regard the conservative estimate of error bars as appropriate, at least for the deeper layers.

The composition of the buckled layer in the LEED analysis is 50 at. %, indicating a depletion in Au with respect to the bulk. Regarding the error limits, a range from 25–85 at. % Au is compatible with the data, so even an Au enrichment cannot be excluded.

Regarding the segregation profile, simulations and experiment agree nicely, with perfect agreement for the composition of the first two layers. The third layer composition differs somewhat: The simulations find an enrichment to 83 at. % Au, whereas the experimental data suggest a depletion rather than an enrichment. However, 83 at. % Au are still within the (conservative) error bars for the (experimental) third layer composition.

The deviations from the experimental values may be due to the energy model used in the simulations. The difference in surface energies for Au and Pd may have been assumed too large, which leads to a gold enrichment in deeper layers.

The structure of $Au_3Pd(110)$ is a (1×2) missing-row reconstruction similar to the one found for Au(110). Although no additional structural models other than the missing-row configuration with multilayer relaxations have been tested in the LEED analysis; the agreement between experimental and calculated *I-V* curves is sufficiently convincing that the model is right.

The relaxations found in the first three layers are mostly of the same order as in Au(110).[17,18] The contraction of the first interlayer spacing is $\Delta d_{12}=-13\%$ for $Au_3Pd(110)$, while it is $\approx-17\%$ for Au(110) according to recent studies,[18] with ranges from $+14\%$ to -22% being found in the literature.[18] Also a third layer buckling of 0.14 ± 0.04 Å is found in the present study, similar to the 0.12–0.24 Å found for Au(110).[17,18] The pairing $\Delta y_2=0.015\pm0.07$ Å in the second layer is very small and within the error limits of the analysis, again comparable to the 0.00–0.12 Å for Au(110). A pairing and buckling in the deeper layers has not been allowed in the present study.

According to LEED, the second interlayer spacing shows no significant relaxation, and the expansion by 1% (with respect to the center-of-mass plane in layer three) is within the error limits of the present analysis. For Au(110) an expansion by 2–7 % has been found.[18] This difference is not surprising, since in the alloy the third layer contains around 50 at. % Pd atoms, which will influence the relaxation.

Also, with respect to these structural relaxations, the experimental results for $Au_3Pd(110)$ and the MC-EAM simulations agree rather well. The simulations find relaxations $\Delta d_{12}=-9\%$ and $\Delta d_{23}=1\%$ and a buckling of 0.03 Å in the third layer. No relaxations were found between deeper layers.

Finally, we note that we do not find any evidence for a chemically ordered surface region. No additional spots were present in the LEED pattern, and the XRD measurements indicate bulk disorder. The latter is also found in the simulations. The item of bulk ordering has so far not conclusively been discussed in the literature. Whereas some phase diagrams[42] show only a solid-solution phase, others[43] indicate also a chemically ordered $L1_2$ structure for Au_3Pd. To our knowledge, there is only one study claiming chemical order for the Au_3Pd alloy,[44] and this study has been performed on evaporated films of Au and Pd that have been subsequently alloyed by heating. Another study[45] on similarly prepared Au_3Pd films found no ordered phase. No ordering has been found for bulk samples so far, which is in agreement with our results.

The evolution of the calculated segregation profiles as a function of temperature is perfectly normal: at higher temperature both the extent of segregation and the compositional oscillations are somewhat less pronounced due to the increasing importance of entropy at higher temperatures. For future experiments it will be intriguing to study the temperature behavior of the surface composition and structure, since the Au(110) surface undergoes a $(1\times2)\leftrightarrow(1\times1)$ phase transition at about 650 K.[46,47] Simulations at 800 K with the relaxations quoted above suggest that the (1×2) missing-row reconstruction remains stable at least up to this temperature.

V. SUMMARY

The structure and composition of the $Au_3Pd(110)$ surface have been determined by quantitative LEED and LEIS. The experimental results are compared with MC-EAM simulations of the structure and the segregation profile of the first few atomic layers.

In the LEED analysis, we find a (1×2) missing-row reconstruction with multilayer relaxations, similar to Au(110). The first interlayer spacing is 1.23 ± 0.04 Å, i.e., contracted (-13%) with respect to the bulk spacing of 1.418 Å ($a_0=4.01$ Å, as measured by XRD). In the second layer a slight pairing by 0.015 ± 0.07 Å has been found, together with a buckling by 0.14 ± 0.04 Å in the third layer. Referring to the center-of-mass plane in layer three, the second interlayer spacing d_{23} is 1.43 ± 0.04 Å, corresponding to a small expansion by 1% compared to the bulk. The third interlayer distance is $d_{34}=1.41\pm0.04$ Å, equal to the bulk spacing.

LEED and LEIS indicate strong Au segregation, with a topmost layer concentration of 100 at. % Au. The LEED data indicate also 100 at. % Au in the second layer and 50 at. % Au in the third layer. The calculated segregation profile is in perfect agreement with the experimental data for the two topmost layers (first layer, 96 at. % Au; second layer, 94 at. % Au). Only in the third layer an enrichment to 83 at. % Au has been found, contrary to the depletion found by LEED. This could be due to an underestimation of the calculated mixing energy, which would exaggerate the Au content in the third layer.

The relaxations found in the calculations agree nicely with the experimental data, indicating a significant contraction of the first interlayer spacing, a slight expansion between the second and third layer, and a small buckling in the third layer. With increasing temperature up to 800 K, the calculated segregation effects become somewhat less pronounced as can be expected.

ACKNOWLEDGMENTS

Financial support by the Deutsche Forschungsgemeinschaft (DFG), the Deutsche Akademische Austauschdienst (DAAD, Vigoni-Program), and the ESF is gratefully acknowledged. This work was partially supported by MURST and CNR.

[1] R. L. Moss and L. Whalley, *Advances in Catalysis* (Academic Press, New York, 1983), Vol. 22, p. 115.
[2] J. H. Sinfelt, *Bimetallic Catalysts: Discoveries, Concepts and Applications* (Wiley, New York, 1983).
[3] F. Besenbacher, I. Chorkendorff, B. S. Clauesn, B. Hammer, A. M. Molenbroek, J. K. Nørskov, and I. Stensgaard, Science **279**, 1913 (1998).
[4] H. Niehus, Phys. Status Solidi B **192**, 357 (1995).
[5] L. Houssiau and P. Bertrand, Nucl. Instrum. Methods Phys. Res. B **125**, 328 (1997).
[6] S. Schömann and E. Taglauer, Surf. Rev. Lett. **3**, 1823 (1996).
[7] A. Piaszenski, M. Aschoff, S. Speller, and W. Heiland, Nucl. Instrum. Methods Phys. Res. B **135**, 331 (1998).
[8] M. Aschoff, S. Speller, J. Kuntze, W. Heiland, E. Platzgummer, M. Schmid, P. Varga, and B. Baretzky, Surf. Sci. **415**, L1051 (1998).
[9] J. Kuntze, A. Atrei, S. Speller, G. Rovida, W. Heiland, and U. Bardi, Phys. Rev. B **60**, 1535 (1999).
[10] M. A. Van Hove, R. J. Koestner, P. C. Stair, J. P. Bibérian, L. L. Kesmodel, I. Bartovs, and G. A. Somorjai, Surf. Sci. **103**, 189 (1981).
[11] W. Hebenstreit, G. Ritz, M. Schmid, A. Biedermann, and P. Varga, Surf. Sci. **388**, 150 (1997).
[12] G. Ritz, M. Schmid, P. Varga, A. Borg, and M. Rønning, Phys. Rev. B **56**, 10 518 (1997).
[13] E. Platzgummer, M. Sporn, R. Koller, M. Schmid, W. Hofer, and P. Varga, Surf. Sci. **423**, 134 (1999).
[14] R. Baudoing-Savois, Y. Gauthier, and W. Moritz, Phys. Rev. B **44**, 12 977 (1991).
[15] P. Fery, W. Moritz, and D. Wolf, Phys. Rev. B **38**, 7275 (1988).
[16] W. Moritz and D. Wolf, Surf. Sci. **88**, L29 (1979).
[17] W. Moritz and D. Wolf, Surf. Sci. **163**, L655 (1985).
[18] Ch. Höfner and J. W. Rabalais, Surf. Sci. **400**, 189 (1998).
[19] A. Barbieri and M. A. Van Hove, *Symmetrized Automated Tensor LEED Package, Version 4.1*.
[20] A. Barbieri and M. A. Van Hove (private communication).
[21] C. Kittel, *Einführung in die Festkörperphysik*, 9th ed. (Oldenbourg, München, 1991).
[22] S. Crampin and P. J. Rous, Surf. Sci. Lett. **244**, L137 (1991).
[23] M. A. Van Hove, W. H. Weinberg, and C.-M. Chan, *Low-Energy Electron Diffraction*, edited by G. Ertl and R. Gomer, Springer Series in Surface Sciences Vol. 6 (Springer-Verlag, Berlin, 1986).
[24] J. B. Pendry, J. Phys. C **13**, 937 (1980).
[25] E. Taglauer, Appl. Phys. A: Solids Surf. **38**, 161 (1985).
[26] P. Varga and G. Hetzendorf, Surf. Sci. **162**, 544 (1985).
[27] H. Niehus, W. Heiland, and E. Taglauer, Surf. Sci. Rep. **17**, 213 (1993).
[28] N. Metropolis, A. W. Rosenbluth, M. N. Rosenbluth, A. H. Teller, and E. Teller, J. Chem. Phys. **21**, 1087 (1953).
[29] D. W. Heermann, *Computer Simulation Methods in Theoretical Physics* (Springer-Verlag, Berlin, 1986).
[30] K. Binder, *Topics in Current Physics* (Springer-Verlag, Berlin, 1984), Vol. 36, Chap. 1, pp. 1–36.
[31] K. Binder, *Topics in Current Physics* (Springer-Verlag, Berlin, 1979), Vol. 7, Chap. 1, pp. 1–45.
[32] *Lecture Notes in Physics*, edited by W. G. Hoover, I. H. Araki, K. Hepp, R. Kippenhahn, H. A. Weidenmüller, and J. Zittart (Springer-Verlag, Berlin, 1986), Vol. 258, pp. 42–71.
[33] C. Creemers and P. Deurinck, Surf. Interface Anal. **25**, 177 (1997).
[34] P. Deurinck and C. Creemers, Surf. Sci. **419**, 62 (1998).
[35] S. M. Foiles, Phys. Rev. B **32**, 7685 (1985).
[36] S. M. Foiles, M. I. Baskes, and M. S. Daw, Phys. Rev. B **33**, 7983 (1986).
[37] E. Clementi and C. Roetti, At. Data Nucl. Data Tables **14**, 177 (1974).
[38] A. D. McLean and R. S. McLean, At. Data Nucl. Data Tables **26**, 197 (1981).
[39] J. H. Rose, J. R. Smith, F. Guinea, and J. Ferrante, Phys. Rev. B **29**, 2963 (1984).
[40] F. L. Williams and D. Nason, Surf. Sci. **45**, 377 (1974).
[41] M. Sporn, E. Platzgummer, S. Forsthuber, M. Schmid, W. Hofer, and P. Varga, Surf. Sci. **416**, 423 (1998).
[42] *Metal Reference Book*, 5th ed., edited by C. J. Smith (Butterworths, London, 1976).
[43] H. Okamoto and T. B. Massalski, Bull. Alloy Phase Diagrams **6**, 229 (1985).
[44] A. Nagasawa, Y. Matsuo, and J. Kakinoki, J. Phys. Soc. Jpn. **20**, 1881 (1965).
[45] Y. Kawasaki, S. Ino, and S. Ogawa, J. Phys. Soc. Jpn. **30**, 1758 (1971).
[46] J. C. Campuzano, M. S. Foster, G. Jennings, R. F. Willis, and W. Unertl, Phys. Rev. Lett. **54**, 2684 (1985).
[47] H. Derks, W. Hetterich, E. Van de Riet, H. Niehus, and W. Heiland, Nucl. Instrum. Methods Phys. Res. B **48**, 315 (1990).